Journal of Solid State Chemistry 184 (2011) 304–311

Contents lists available at ScienceDirect

Journal of Solid State Chemistry

journal homepage: www.elsevier.com/locate/jssc

CO_2 capture properties of M–C–O–H (M=Li, Na, K) systems: A combined density functional theory and lattice phonon dynamics study

Yuhua Duan [a,*], Bo Zhang [a,b], Dan C. Sorescu [a], J. Karl Johnson [a,b]

[a] United States Department of Energy, National Energy Technology Laboratory, Pittsburgh, PA 15236, USA
[b] Department of Chemical Engineering, University of Pittsburgh, Pittsburgh, PA 15261, USA

ARTICLE INFO

Article history:
Received 14 May 2010
Received in revised form
23 November 2010
Accepted 1 December 2010
Available online 7 December 2010

Keywords:
CO_2 capture
Density functional theory
Lattice phonon dynamics
Thermodynamics

ABSTRACT

We have computed the phase diagrams for multi-component M–C–O–H (M=Li, Na, K) systems using first-principles density functional theory complemented with lattice phonon calculations. We have identified all CO_2 capture reactions that lie on the Gibbs free energy convex hull as a function of temperature and the partial pressures of CO_2 and H_2O. Our predicted phase diagrams for CO_2 capture reactions are in qualitative and in some instances quantitative agreement with experimental data. The Na_2CO_3/$NaHCO_3$ and K_2CO_3/$KHCO_3$ systems were found to be the most promising candidates of all those we investigated for both pre- and post-combustion CO_2 capture. Overall, we show that our calculation approach can be used to screen promising materials for CO_2 capture under different conditions of temperature and pressure.

Published by Elsevier Inc.

1. Introduction

Carbon dioxide from large stationary sources such as power plants has been identified as one of the leading causes of global warming [1–3]. Carbon-free renewable energy sources are not likely to completely replace fossil fuel power plants for many years to come [4]. Hence, there is a need to reduce CO_2 emission by carbon capture and sequestration so that fossil fuel power plants may be operated without releasing enormous quantities of CO_2 into the atmosphere [5–7]. Current technologies for capturing CO_2 include solvent-based systems (such as MEA, Selexol, and Rectisol), and alkanolamine-based materials (such as ethanolamine). It is generally accepted that operation or regeneration of these materials is too energy intensive [1,2]. Hence, there is critical need for development of new materials that can capture and release CO_2 reversibly with acceptable energy and operating costs. Accordingly, solid sorbent materials have been proposed for capture of CO_2 through a reversible chemical transformation. Among them, regenerable solid sorbents play an important role for CO_2 capture, especially above room temperature ($\sim$100 °C for post-combustion, $\sim$300 °C for pre-combustion) [1,8–15].

There are multiple opportunities to capture carbon in conjunction with power generation. Two of these are post- and pre-combustion capture. In post-combustion capture CO_2 is separated from the flue gas from a power plant. The flue gas is typically at low pressure (just over atmospheric) and moderate temperature ($<$100 °C). The concentration of CO_2 in flue gas is 10–15% by volume. The second option is to capture CO_2 at the pre-combustion stage, as in gasification-type power generation such as in the integrated gasification combined cycle (IGCC). In this scenario, a fossil fuel such as coal or biomass is converted to synthesis gas, from which CO_2 can be captured before being mixed with air in a combustion turbine. The concentration of CO_2 in the pre-combustion stream is typically at a pressure of 15–20 bar and temperatures 250–300 °C.

In this paper, we assess the suitability of solid sorbents containing alkali metals for capturing CO_2 from both post- and pre-combustion streams using a theoretical approach. These materials have previously been investigated [1,14,16–20]. Alkali metal oxides and hydroxides have attracted interest because of their ability to absorb high weight percentages of CO_2 at moderate working temperatures [21]. Moreover, experimental studies indicate that mixtures of hydroxides with oxides can improve the CO_2 absorption performance [14,17].

There have been very few theoretical studies of CO_2 reactions with alkali oxides and hydroxides up to this point. In contrast, there are many experimental studies on this topic [21,22]. Based on thermodynamic data, Feng et al. [23] analyzed 11 simple metal oxides and concluded that CaO is thermodynamically the best candidate among them for CO_2 capture in zero emission power generation systems. Based on the density functional theory (DFT), Jensen et al. [24] investigated the CO_2 adsorption on CaO and MgO surfaces. Their results showed that CO_2 adsorbs as monodentate on edge sites and bidentate on corner sites of MgO. In contrast, CO_2 adsorbs as monodentate on both edge and corner sites of CaO.

* Corresponding author. Fax: +1 412 386 5920.
E-mail address: yuhua.duan@netl.doe.gov (Y. Duan).

0022-4596/$ - see front matter Published by Elsevier Inc.
doi:10.1016/j.jssc.2010.12.005

Recently, Duan and Sorescu proposed a methodology to identify promising solid sorbent candidates for CO_2 capture by combining DFT total energy calculations with lattice phonon dynamics [19,20,25]. For Li_2O solid, it was concluded that although pure Li_2O can absorb CO_2 efficiently, it is not a good solid sorbent for CO_2 capture because the reverse reaction, corresponding to Li_2CO_3 releasing CO_2, can only occur at very low CO_2 pressure or at very high temperature when Li_2CO_3 is in the liquid phase [19]. These predicted results are in very good agreement with experimental measurements [26]. In this study, we apply our previously developed computational methodology to systems containing alkali metal oxides, hydroxides, and carbonates to explore their CO_2 capture properties systematically. We present a linear programming approach to identify the families of reactions that lie on the convex hull of the Gibbs free energy for the *M*–C–O–H systems for *M*=Li, Na, and K. In this work we consider solid phases consisting of only the oxides, hydroxides, carbonates, and bicarbonates. We compare our predictions with available thermodynamic data to assess the accuracy of our approach.

2. Theoretical methods

To determine phase diagrams of multi-component systems, we assume that all possible solid phases are in contact with a gas-phase reservoir having specified partial pressures of CO_2 and H_2O. The grand-canonical Gibbs free energy of such system can be written as [27]

$$G(T,\mu_{\text{gas}}) = \sum_{j=1}^{S} x^j F^j(T) - \sum_{j=1}^{S} \mu^{j,\text{gas}}(T,p) x^{j,\text{gas}} \tag{1}$$

where $F^j(T)$ is the free energy of solid phase "j" (ignoring the pV term contribution), S is the number of solid substances, $\mu^{j,\text{gas}}(T,p)$ is the chemical potential of gas species, x^j is the unknown mole fraction of phase j coexisting at a given composition, temperature, and pressure. The molar fraction x^j is based on elements appearing only as solids (in this case only the metals).

The x^j mole fractions are determined by minimizing the grand-canonical Gibbs free energy, subject to the following mass-conservation constraints for the solid phase species

$$\sum_{i=\text{metal}}^{M} f_i = \sum_{i=\text{metal}}^{M} \sum_{j=1}^{S} x^{j,\text{solid}} b_i^{j,\text{solid}} = 1 \tag{2}$$

where f_i is the molar ratios of solid element i, $b_i^{j,\text{solid}}$ represents the number of atoms of type i in one formula unit of phase j, and M is the number of elements. These two equations form a linear programming problem that can be solved using existing techniques. The conditions at which a chemical reaction occurs can be identified by comparing the mole fractions x^j at two consecutive temperature or pressure steps. If x^j values change then a reaction occurred between the temperature or pressure interval. We can choose sufficiently small intervals of temperature and pressure to ensure adequately small chemical potential changes between two steps in order to guarantee single step reactions. The change in the Gibbs free energy of the system due to a reaction is zero at thermodynamic equilibrium and can be calculated by

$$\Delta G = 0 = \Delta F_{\text{solid}} + \sum n_g \mu_g \tag{3}$$

where n_g is the number of moles of gas molecules g consumed or released as a result of the reaction. The locus of points that satisfy Eq. (3) as a function of temperature and pressure define the equilibrium phase diagram.

The chemical potentials of CO_2 (μ_{CO_2}) and H_2O (μ_{H_2O}) required in Eqs. (1) and (3) can be obtained from standard statistical mechanics (assuming ideal gas behavior):

$$\mu_{CO_2}(T,p) \approx E_{CO_2}^{\text{DFT}} + \frac{7}{2}RT + \sum_{i=1}^{4} \frac{N_a h\nu_i}{e^{-h\nu_i/kT}-1} - TS_{CO_2}(T) - n_{CO_2} RT \ln\left(\frac{p_{CO_2}}{P_0}\right) \tag{4}$$

$$\mu_{H_2O}(T,p) \approx E_{H_2O}^{\text{DFT}} + 4RT + \sum_{i=1}^{3} \frac{N_a h\nu_i}{e^{-h\nu_i/kT}-1} - TS_{H_2O}(T) - n_{H_2O} RT \ln\left(\frac{p_{H_2O}}{P_0}\right) \tag{5}$$

where N_a is Avogadro's constant. The entropy of CO_2 ($S_{CO_2}(T)$) and H_2O ($S_{H_2O}(T)$) can be accurately calculated from the Shomate equation [28]. The vibrational frequencies (ν_i) of CO_2 are 673 cm^{-1}(π_u), 1354 cm^{-1}(σ_g^+), and 2397 cm^{-1}(σ_u^+) [29], and the vibrational frequencies (ν_i) of H_2O are 3657.05 cm^{-1} (ν_1), 1594.75 cm^{-1}(ν_2), and 3755.93 cm^{-1}(ν_3) [30]. The zero point energies for CO_2 and H_2O calculated using these frequencies are 0.3160 and 0.5584 eV, respectively.

The free energy of each solid phase ($F^j(T)$ in Eq. (1)) can be computed from

$$F(T) = E^{\text{DFT}} + F_{\text{harm}}(T) \tag{6}$$

where E^{DFT} is the total energy of each solid calculated from DFT. We have used the Vienna *Ab-initio* Simulation Package (VASP) [31,32] to calculate the electronic structures and the total energies of all solid materials. All calculations employed projector augmented wave pseudo-potentials [33] and the PW91 exchange-correlation functional [34]. A planewave energy cutoff of 500 eV and an augmentation charge cutoff of 605.4 eV were used in all calculations. The Monkhorst–Pack method [35] was used to generate the k-point grids. A sufficient number of k-points was used to ensure a spacing of about 0.028 $Å^{-1}$ along the axes of the reciprocal unit cells. Both the unit cell dimensions and the positions of the atoms in the cell were relaxed to the equilibrium configurations. The energies of CO_2 and H_2O molecules ($E_{CO_2}^{\text{DFT}}$ and $E_{H_2O}^{\text{DFT}}$ in Eqs. (4) and (5)) are computed to be −22.99409 and −14.27267 eV, respectively, as determined from calculations of an isolated molecule in a cubic box with a length of 20 Å.

The terms $F_{\text{harm}}(T)$ and $S_{\text{harm}}(T)$ in Eq. (6) are the phonon free energy and entropy of each solid phase, which are defined as [36–38]

$$F_{\text{harm}}(T) = rk_BT \int_0^\infty g(\omega) \ln\left[2\sinh\left(\frac{\hbar\omega}{2k_BT}\right)\right] d\omega \tag{7}$$

$$S_{\text{harm}}(T) = rk_B \int_0^\infty g(\omega) \left\{ \left(\hbar\frac{\hbar\omega}{2k_BT}\right)\left[\coth\left(\frac{\hbar\omega}{2k_BT}\right)-1\right] - \ln\left[1-\exp\left(-\frac{\hbar\omega}{k_BT}\right)\right]\right\} d\omega \tag{8}$$

$$E_{\text{tot}}(T) = \frac{1}{2} r \int_0^\infty g(\omega)(\hbar\omega)\coth\left(\frac{\hbar\omega}{2k_BT}\right) d\omega \tag{9}$$

where r is the number of degrees of freedom in the primitive unit cell, ω is the phonon dispersion frequency, and $g(\omega)$ is the phonon density of states. It can be seen that the zero-point-energy (E_{ZP}) can be obtained from Eq. (9) by taking $T \to 0$:

$$E_{ZP} = \lim_{T\to 0}(E_{\text{tot}}(T)) \tag{10}$$

In this study, the phonon properties were evaluated using the direct method within the harmonic approximation as implemented in the PHONON software package [39] following the formalism derived by Parlinski et al. [37]. A supercell of at least $2 \times 2 \times 2$ unit cells was used in all phonon calculations. Structures with displacements of 0.03 Å of the non-equivalent atoms were generated from the optimized supercell and DFT calculations were performed to

obtain the forces on each atom due to these displacements. These forces were input into the PHONON package [39] to fit the force constant matrix and to compute the phonon density of states. These were then used in Eqs. (7)–(9) to calculate the thermodynamic properties. The symbols and coordinates of the high symmetry points in the first Brillouin zone of the crystals were taken from Bradley and Cracknell's definitions [40] in the phonon dispersion calculations.

The enthalpy change for the reaction of CO_2 capture, $\Delta H^{cal}(T)$, can be derived from above equations as [38]

$$\Delta H^{cal}(T) = \Delta G^{cal}(T) + T\left[n_{CO_2} S_{CO_2}(T) + n_{H_2O} S_{H_2O}(T) + \Delta S^{solid}_{harm}(T)\right] \quad (11)$$

where $\Delta G^{cal}(T)$ is the Gibbs free energy change for the reaction, while $\Delta S^{solid}_{harm}(T)$ is the entropy difference between the product and the reactant solids. If H_2O is a product, n_{H2O} takes a negative value.

We have used the HSC Chemistry package [41] to generate thermodynamic data for comparison with our first-principles predictions. The HSC Chemistry package data are based on fits of experimental thermodynamic values to analytical polynomials. We have also used tabulated values of the heats of formation from the JANAF tables [28] to compute thermodynamic equilibrium data for comparison with our theoretical calculations.

3. Results and discussions

3.1. DFT and phonon calculated results

The optimized lattice constants and total electronic energies for the 12 alkali metal oxides, hydroxides, bicarbonates, and carbonates considered in this work are shown in Table 1, along with experimental structural data. It was reported that $LiHCO_3$ is not stable in the solid phase and exists only in solution [42]. For this reason, we assumed that the crystal structure of $LiHCO_3$ at low temperatures has the same symmetry as the $NaHCO_3$ crystal and therefore used data for $NaHCO_3$ as its initial structure to obtain an

Table 1
Comparison of the experimental and DFT calculated structural parameters for the compounds in the reactions studied, with all distances in angstroms and angles in degrees. Although calculations are performed on several phases of each compound, only the lowest energy phase, determined by DFT total energy, is listed. The zero-point energy and entropy calculated from phonon density of states, as well as the experimental data are also listed.

Compound	Space group	Structural parameters		Calculated energy (eV/f.u.)		Entropy (J/mol K)		Heat of formation (eV/f.u.)	
		Experimental	calculated	E^{DFT}	E_{ZP}	Calc. (T=300 K)	Exp. (298 K)[a]	Calc. (T=0 K)	Exp. (T=298 K)
Li_2O[b]	$Fm\bar{3}m$ (no. 225) [48]	a=4.62	a=4.63157	−14.43538	0.23628	38.468	37.61	−5.68056	−6.19680
Na_2O	$Fm\bar{3}m$ (no. 225) [49]	a=5.55	a=5.58517	−11.34789	0.12801	76.843	75.04	−3.81274	−4.29288
K_2O	$Fm\bar{3}m$ (no. 225) [50]	a=6.436	a=6.52362	−10.14413	0.08048	112.137	94.10	−3.15256	−3.74668
LiOH	$P4/nmmS$ (no. 129) [51]	a=3.549 c=4.334	a=3.55985 c=4.41752	−15.01799	0.41897	37.015	42.81	−4.67909	−5.05258
NaOH	$Cmcm$ (no. 63) [44]	a=3.4013 b=3.3984 c=11.378	a=3.43101 b=3.41409 c=11.39869	−13.72285	0.36924	60.556	64.43	−3.98383	−3.98383
KOH	$P12_1/m1$ (no. 11) [44]	a=3.957 b=3.995 c=5.742 β=103.93°	a=4.01060 b=4.02644 c=5.93073 β=103.47°	−13.38330	0.33355	62.591	81.25	−3.95017	−4.40067
Li_2CO_3[b]	$C2/c$ (no. 15) [52]	a=8.35884 b=4.97375 c=6.19377 β=114.789°	a=8.40532 b=5.02789 c=6.29445 β=114.16°	−39.55190	0.59912	93.615	90.169	−11.66566	−12.60192
Na_2CO_3	$C12/m1$ (no. 12) [53]	a=9.01029 b=5.23116 c=6.34548 β=96.062°	a=8.95180 b=5.33507 c=6.13861 β=102.21°	−37.29272	0.49152	122.534	138.783	−10.64579	−11.71888
K_2CO_3	$P12_1/c1$ (no. 14) [52]	a=5.63961 b=9.8312 c=6.83407 β=98.703°	a=5.76055 b=9.90478 c=7.18110 β=97.30°	−36.90480	0.45733	160.121	155.50	−10.78310	−11.92928
$LiHCO_3$	$P12_1/c1$ (no. 14)	No exp. data available. Symmetry taken same as $NaHCO_3$	a=3.90035 b=9.06555 c=7.76529 β=115.54°	−38.79546	0.81407	88.890		−9.29722	
$NaHCO_3$	$P12_1/c1$ (no. 14) [54]	a=3.51 b=9.71 c=8.05 β=111.85°	a=3.54929 b=9.79559 c=8.12575 β=112.82°	−38.01484	0.78150	103.956	101.70	−9.85435	−9.85435
$KHCO_3$	$P12_1/a1$ (no. 14) [55]	a=15.1725 b=5.6283 c=3.711 β=104.631°	a=15.46219 b=5.73344 c=3.79398 β=105.71°	−37.88604	0.76068	122.406	115.499	−9.25403	−9.98287
CO_2 molecule	$P_1(D_{\infty h})$	r_{C-O}=1.163	r_{C-O}=1.1755	−22.99409	0.31598		213.388	−3.89536	−4.07834
H_2O molecule	$P_1(C_{2v})$	r_{O-H}=0.957 ∠HOH=104.4°	r_{O-H}=0.9714 ∠HOH=104.2°	−14.27267	0.55841		188.832	−2.35015	−2.50608

[a] Taken from HSC Chemistry Package [41].
[b] Taken from Ref. [19].

estimate for the optimized structure. Some of the compounds in Table 1 have more than one reported crystal phase. We have computed the energies of each of the different crystal structures, but only the lowest energy structures (at $T=0$ K) are reported in Table 1. The agreement between the DFT optimized lattice constants and experimental data are generally very good, as can be seen from Table 1. The calculated heats of formation (ΔH_f^0) at $T=0$ K as well as the experimental value at room temperature for each compound are also shown in Table 1.

Phonon calculations were performed for each solid compound shown in Table 1. The finite temperature thermodynamic properties were then computed from these data. As an example, the calculated phonon free energy and entropy for the solid phase materials in the Na–C–O–H system are plotted as a function of temperature in Fig. 1. The zero-point energy (E_{ZP}) of each compound, calculated from Eq. (10), is also shown in Table 1.

From Table 1, one can see that the calculated entropies of these oxides, hydroxides and carbonates are in good agreement with the experimentally measured values. Additionally, our calculated electronic properties and phonon dispersion relations (not shown) are also in good agreement with data from the literature for oxides and carbonates [43].

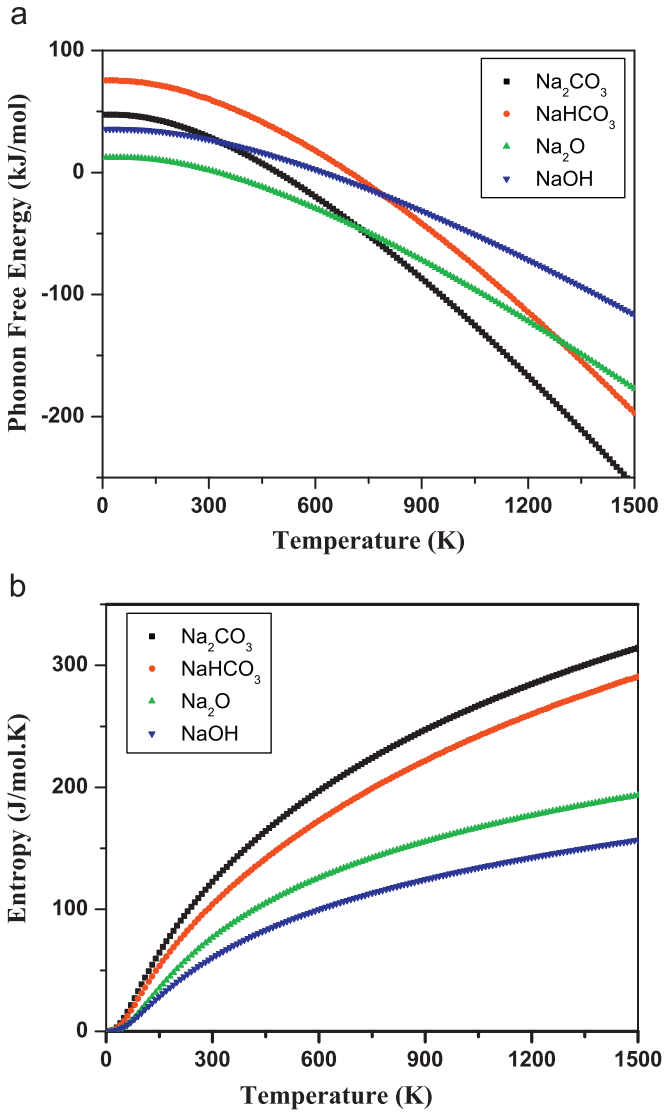

Fig. 1. Calculated phonon free energies (a) and entropies (b) for various solids in the Na–C–O–H system as a function of temperature.

3.2. Phase diagrams of M–C–O–H systems

The calculated phase diagrams of M–C–O–H for M=Li, Na, and K are shown in Figs. 2(a), 3(a), and 4(a), respectively. The three independent variables in the phase diagram are the temperature, the partial pressure of CO_2 and the partial pressure of H_2O. The surfaces shown in the figures correspond to chemical reactions (phase transitions), which are identified in the legends of the graphs. The following general features can be seen from Figs. 2(a), 3(a), and 4(a): at low temperature and high CO_2 pressure, the most stable phase is $MHCO_3$. When the temperature is increased, $MHCO_3$ is converted to carbonate, M_2CO_3, which is stable over quite wide ranges of temperature and pressure. The MOH phase is stable at low CO_2 partial pressure, high H_2O partial pressure, and lower temperatures. At very high temperatures and low CO_2 partial pressure, the M_2O phase is stable.

The calculated heats of reaction and free energies of reaction for nine reactions involving capture of CO_2 are given in Table 2, along with the corresponding data from the HSC Chemistry package [41]. The partial pressures of CO_2 and H_2O are set to 1 bar in the finite temperature calculations. The calculated heats of reaction (ΔH) for the carbonate to bicarbonate reactions are shown in Fig. 5 as a function of temperature along with data from the HSC chemistry package. The calculated heats of reactions and Gibbs free energy changes (ΔG) at 300 K are given in Table 2. The DFT data deviate by about 15–25 kJ/mol from the HSC data for the CO_2 capture reactions involving alkali metal oxides and hydroxides. However,

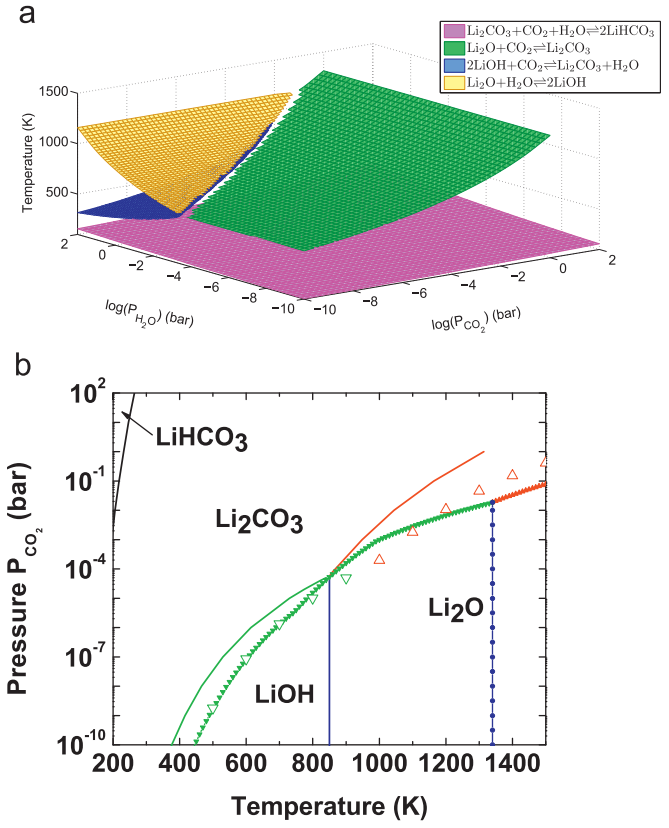

Fig. 2. The calculated phase diagram of Li–O–C–H systems with the relationships of T, P_{CO_2} and P_{H_2O}: (a) three dimensional plot; (b) two dimensional plot at fixed $P_{H_2O}=1$ bar. Solid lines represent the phase boundary calculated from DFT. For comparison, the available experimental data from the HSC Chemistry package [41] (solid lines, filled symbols) and JANAF tables [28] (open symbols) are also potted. Phases are labeled according to our DFT results, boundaries are colored. Black: $Li_2CO_3+CO_2 \rightleftharpoons 2LiHCO_3$; Red: $Li_2O+CO_2 \rightleftharpoons Li_2CO_3$; Green: $2LiOH+CO_2 \rightleftharpoons Li_2CO_3+H_2O$; Blue: $Li_2O+H_2O \rightleftharpoons 2LiOH$ (for interpretation of the references to color in this figure legend, the reader is referred to the web version of this article).

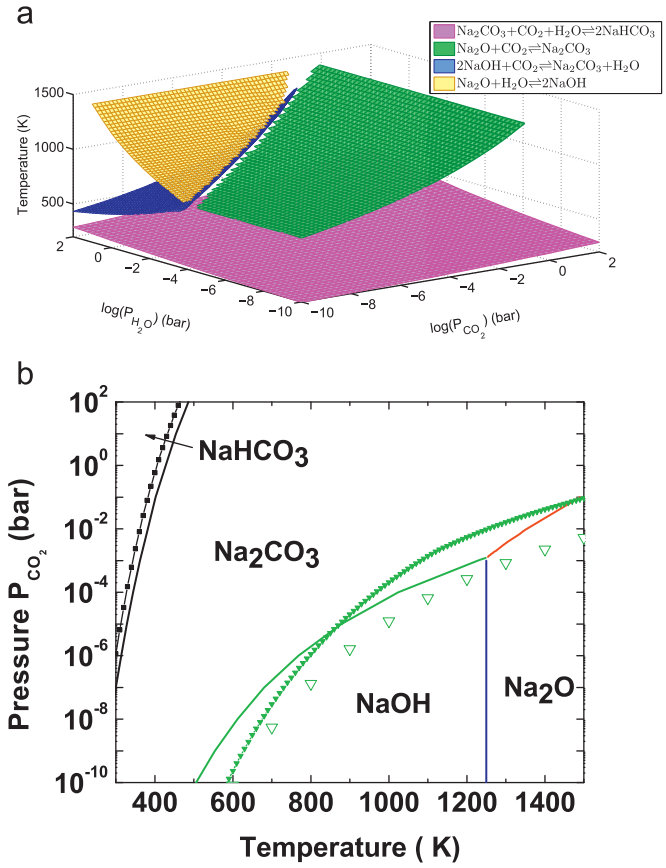

Fig. 3. The calculated phase diagram of Na–O–C–H systems with the relationships of T, P_{CO_2}, and P_{H_2O}: (a) three dimensional plot and (b) two dimensional plot at fixed $P_{H_2O} = 1$ bar. Solid lines represent the phase boundary calculated from DFT. For comparison, the available experimental data from the HSC Chemistry package (solid lines, filled symbols) and JANAF tables (open symbols) are also potted. Phases are labeled according to our DFT results, boundaries are colored. Black: $Na_2CO_3+CO_2 \rightleftharpoons 2NaHCO_3$; Red: $Na_2O+CO_2 \rightleftharpoons Na_2CO_3$; Green: $2NaOH+CO_2 \rightleftharpoons Na_2CO_3+H_2O$; Blue: $Na_2O+H_2O \rightleftharpoons 2NaOH$ (for interpretation of the references to color in this figure legend, the reader is referred to the web version of this article).

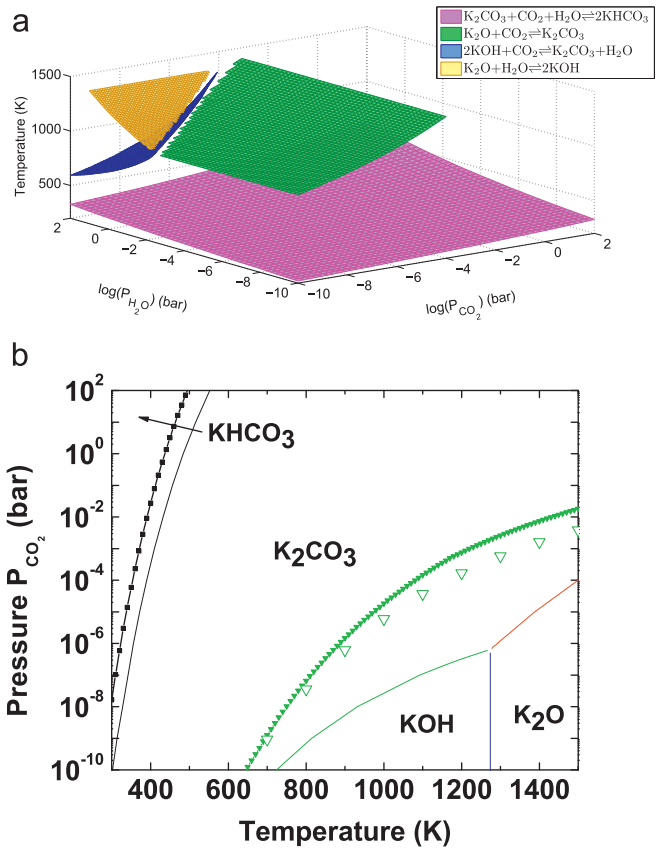

Fig. 4. The calculated phase diagram of K–O–C–H systems with the relationships of T, P_{CO_2}, and P_{H_2O}: (a) three dimensional plot; (b) Two dimensional plot at fixed $P_{H_2O} = 1$ bar. Solid lines represent the phase boundary calculated from DFT. For comparison, the available experimental data from the HSC Chemistry package (solid lines, filled symbols) and JANAF tables (open symbols) are also potted. Phases are labeled according to our DFT results, boundaries are colored. Black: $K_2CO_3+CO_2 \rightleftharpoons 2KHCO_3$; Red: $K_2O+CO_2 \rightleftharpoons K_2CO_3$; Green: $2KOH+CO_2 \rightleftharpoons K_2CO_3+H_2O$; Blue: $K_2O+H_2O \rightleftharpoons 2KOH$ (for interpretation of the references to color in this figure legend, the reader is referred to the web version of this article).

reactions involving $M_2CO_3/MHCO_3$ (M=Na, K) show much better agreement with the HSC data, deviating by a few kJ/mol.

In order more easily visualize the effect of CO_2 partial pressure, we fixed $p_{H_2O} = 1$ bar and have plotted the corresponding two-dimensional slices from Figs. 2(a), 3(a), and 4(a) in Figs. 2(b), 3(b), and 4(b). We have also plotted the reactions from the HSC Chemistry database [41] and the JANAF tables [28] in Figs. 2(b), 3(b), and 4(b) in order to compare our DFT calculations with the pseudo-experimental data. Since there are no experimental data for $LiHCO_3$, only the DFT calculated curve for the $LiHCO_3/Li_2CO_3$ reaction is shown in Fig. 2(b). We see from our calculations that $LiHCO_3$ is predicted to exist only at low temperatures and at high CO_2 pressure, e.g. at T=273 K and $p_{CO_2} > 10^2$ bar. This may explain why solid $LiHCO_3$ has not been observed experimentally at ambient conditions. It would be interesting to carry out high pressure experiments to see if $LiHCO_3$ could be observed.

Overall, from Figs. 2, 3, and 4 one can see that the $MHCO_3/M_2CO_3$ reactions for M=Na, K are in reasonably good agreement with the HSC data. However, we note that for other reactions our predictions are not always in good agreement with the HSC data. For the Li system (Fig. 2) we note that the phase boundary from LiOH to Li_2O is predicted to occur at 850 K from the DFT calculations and 1340 K from HSC data. Note, however, that the JANAF tables indicate that the phase transition occurs somewhere between 900 and 1000 K. For the Na system (Fig. 3), our DFT calculations overestimate the pressure for the $NaOH/Na_2CO_3$ reaction at low temperatures and underestimate the pressure for $T > 850$ K. Our DFT data predict that the Na_2O/Na_2CO_3 reaction will occur for $T > 1250$ K, whereas both HSC and JANAF data indicate that NaOH is still the lowest energy phase up to temperatures of 1500 K. Overall, our DFT calculations are in better agreement with the JANAF data than the HSC data for both Li and Na. Note that the HSC and JANAF data are generally in good agreement for $T < 800$ K for both Li and K systems. However, for the Na system there is disagreement between HSC and JANAF data, even at T=700 K. One possible reason for this discrepancy may be due to differences in the melting points of the materials. We give the experimentally reported melting temperatures of the compounds of interest in this work in Table 3. We note from this table that the discrepancy between the HSC and JANAF data roughly correlates with the melting points of the hydroxides. Agreement between HSC and JANAF data for Li and K systems are best below or near the melting points of the hydroxides. NaOH has a very low melting point and gives largest deviation between the JANAF and HSC data. The JANAF data are based on an extrapolation of the solid phase data, since we exclusively used the tables labeled "crystal" in the JANAF tables. This explains the better agreement between our DFT and the JANAF data, since our calculations are based on the assumption that all materials are perfect crystalline solids, except for CO_2 and H_2O. We note that the good agreement between our DFT calculations and HSC data seen

Table 2
The calculated reaction thermodynamics of CO_2 capture by alkali metal oxides, hydroxides and carbonates. Enthalpies and Gibbs free energies correspond to partial pressures of CO_2 and H_2O of 1 bar.

Reactions	CO_2 (wt%)	Calculated thermodynamic properties (kJ/mol)				HSC data at $T=300$ K[a]	
		ΔE^{DFT}	ΔE^{ZP}	$\Delta H^{cal}(T=300\ K)$	ΔG^{cal} $(T=300\ K)$	ΔH (kJ/mol)	ΔG (kJ/mol)
$Li_2O+CO_2\rightleftharpoons Li_2CO_3$	142.52	−204.786	4.521	−200.531	−153.061	−224.643	−176.290
$Na_2O+CO_2\rightleftharpoons Na_2CO_3$	71.01	−284.707	4.586	−282.372	−231.900	−322.153	−277.155
$K_2O+CO_2\rightleftharpoons K_2CO_3$	46.72	−363.424	5.873	−359.308	−309.498	−394.785	−349.084
$2LiOH+CO_2\rightleftharpoons Li_2CO_3+H_2O(g)$	91.88	−76.659	0.348	−72.423	−70.934	−94.567	−88.442
$2NaOH+CO_2\rightleftharpoons Na_2CO_3+H_2O(g)$	55.02	−108.606	-0.437	−108.216	−101.113	−127.510	−122.984
$2KOH+CO_2\rightleftharpoons K_2CO_3+H_2O(g)$	39.22	−136.699	3.151	−127.910	−130.836	−150.711	−141.079
$Li_2CO_3+CO_2+H_2O(g)\rightleftharpoons 2LiHCO_3$	59.56	−74.513	14.918	−65.508	30.287	−86.40[b]	−13.64[b]
$Na_2CO_3+CO_2+H_2O(g)\rightleftharpoons 2NaHCO_3$	41.52	−141.855	19.034	−127.683	−32.415	−135.341	−34.126
$K_2CO_3+CO_2+H_2O(g)\rightleftharpoons 2KHCO_3$	31.84	−154.428	18.293	−141.728	−46.281	−142.854	−44.716

[a] Calculated by the HSC Chemistry package [41].
[b] From Ref. [56].

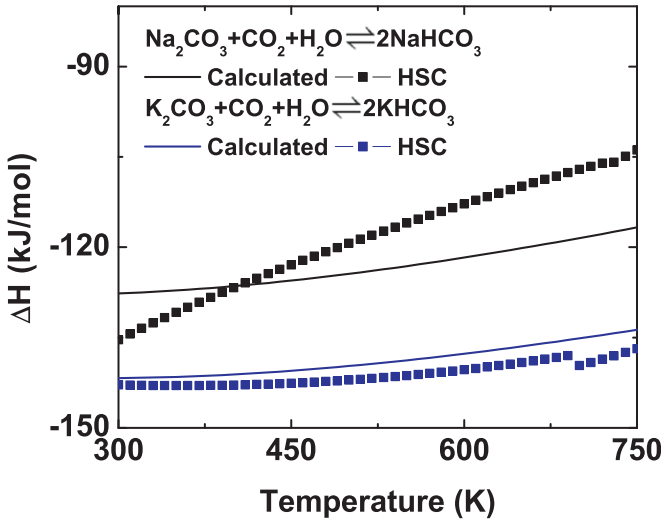

Fig. 5. The calculated heats of reaction as a function of temperature for the carbonate/bicarbonate reactions computed from density functional theory compared with data from the HSC Chemistry package.

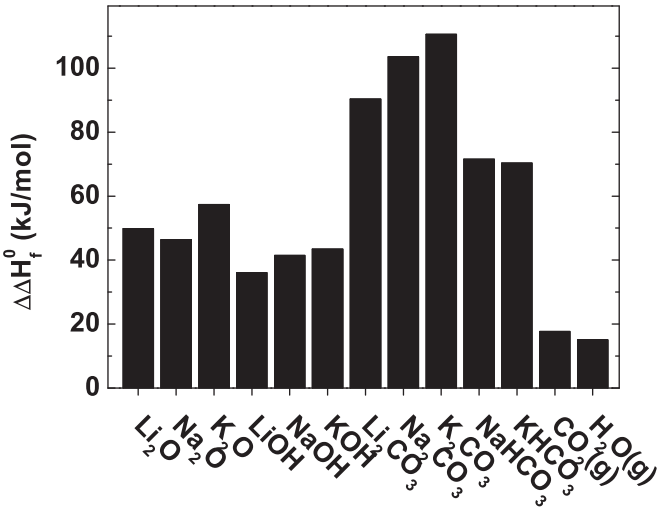

Fig. 6. The relative errors in the calculated heats of formation for compounds studied in this work. We define the relative errors as $\Delta\Delta H_f^0 = \Delta H_f^0(\text{Experimental}) - \Delta H_f^0(\text{DFT})$.

Table 3
Experimental melting points (m. p.) [57] of all available oxides, hydroxides, carbonates, and bicarbonates studied in this work.

Compound	m. p. (K)
Li_2O	1843
Na_2O	1405.2
K_2O	623
LiOH	744.3
NaOH	596
KOH	679
Li_2CO_3	993.15
Na_2CO_3	1123.15
K_2CO_3	1174
$NaHCO_3$	~323
$KHCO_3$	~373

for the $MHCO_3/M_2CO_3$ reactions may be fortuitous. We see from Table 3 that the melting points for the bicarbonates are both below 400 K, so that the bicarbonates would be in the liquid phase for almost the entire range covered in Figs. 2(b), 3(b), and 4(b).

We have explored the origin of the error in our calculations and have found that the heats of formation for many of the compounds we have studied in this work are not in good agreement with experimental data. Fig. 6 presents a comparison of our calculated heats of formation with available experimental data. We see that the error in the DFT calculated heats of formation are very large for the carbonates, being greater than 90 kJ/mol. Note that the bicarbonates also have large errors of about 70 kJ/mol. One reason that the carbonate/bicarbonate reactions are in good agreement with the HSC data are that the total error for the carbonate/bicarbonate reactions are small due to a cancellation of errors. Hence the total errors in the net heats of formation for the $MHCO_3/M_2CO_3$ reactions are about −7 and 3 kJ/mol, for M=Na, K, respectively. In contrast, the errors in the heats of formation for the hydroxide/carbonate reactions are on the order of −20 kJ/mol for all three systems.

We have used the experimental heats of formation along with the DFT calculated finite temperature thermodynamics (zero point energies, entropies, heat capacities) in order to construct the convex hull reaction plots shown in Figs. 2–4. The results for the Li–C–O–H system are shown in Fig. 7 along with the HSC and JANAF data. The other two systems are not shown for brevity. The carbonate/bicarbonate reactions for the Na and K systems (not shown) were only marginally affected by using the experimental heats of reaction, in agreement with the cancellation of errors noted previously. The agreement between the DFT predicted values and the HSC/JANAF data for the Li system is improved when using the experimental heats of formation, as can be seen from Fig. 7. Similar results are seen for the Na system. However, the K–C–O–H

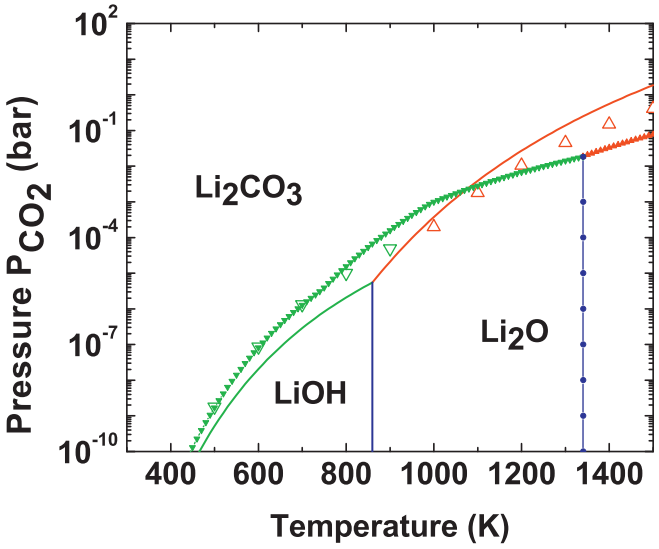

Fig. 7. Phase diagrams computed from DFT but using the experimental heats of formations (solid lines) compared with data from HSC database [41] (solid lines, filled symbols) and JANAF tables [28] (open symbols). Phases are labeled according to our DFT results, boundaries are colored. Red: $Li_2O+CO_2 \rightleftharpoons Li_2CO_3$; Green: $2LiOH+CO_2 \rightleftharpoons Li_2CO_3+H_2O$; Blue: $Li_2O+H_2O \rightleftharpoons 2LiOH$ (for interpretation of the references to color in this figure legend, the reader is referred to the web version of this article).

system (not shown) is not substantially improved by using the experimental heats of formation.

The problem with the K–C–O–H system appears to stem from two issues with the KOH solid phase. Firstly, the crystal structure reported is lacking positions for the H atoms, so we used reasonable guesses for the positions and relaxed the structure to a local ground state. Thus, the structure we used in our calculations may not be the correct ground state structure, although we believe it to be close to the ideal ground state structure. Secondly, and related to the first point, the reason for the lack of H atom positions in the structure is that KOH does not have well defined H atom positions at room temperature because of excessive librational motion of the OH groups in the solid [44]. This means that our ideal solid calculations, which has all H atoms fixed at crystallographic positions, significantly underestimates the entropy of KOH. We see this in Table 1 where the entropy for KOH is underestimated by about 20 J/mol K at 300 K. At higher temperatures we expect the discrepancy to be even larger. In order to investigate the entropic effects due to disorder of the hydrogen atoms we have performed first principles molecular dynamics calculations using the VASP program within a constant temperature ensemble with a set-point temperature of 300 K. We observed a great deal of motion of the H atoms in the system over a time span on the order of 5 ps. This is in qualitative agreement with the experimental claim of OH librational motion at room temperature [44]. We also noted a fair amount of motion of the K cation in the simulation, leading to additional disorder that exacerbates the error in computing the entropy of KOH using a perfect crystal. The underestimation of the KOH entropy appears to be the greatest source of error in the K–C–O–H system, because a comparison of the calculated entropy with tabulated entropy for all MOH (M=Li, Na, K) as a function of temperature shows that the KOH system has much larger errors than either of the other two systems.

In general, errors between the HSC and DFT values persist even when using the experimental heats of formation due to the following assumptions made in our calculations: (1) We assume perfect crystals, whereas at high temperatures the experimental systems may consist of defective crystals or even liquids. (2) We assume that each of the solid compounds remains in its low temperature crystal structure. i.e. we do not account for solid–solid phase transitions for the pure compounds and for lattice expansions with increasing temperature. (3) We use the harmonic approximation to compute the phonon dispersion relations. At high temperatures anharmonic effects will be increasingly important. For liquids the phonon dispersion relations are not valid. Hence, our DFT calculations should be best at lower temperatures, and this is confirmed by the generally good agreement between the pseudoexperimental data and our calculations at low temperatures.

3.3. Application to pre- and post-combustion CO_2 capture technologies

In this section, we consider how our predictions can be used to identify reactions appropriate for capturing CO_2 from pre- and post-combustion streams. Under pre-combustion conditions, after application of the water–gas shift reaction, a fuel gas stream mainly contains CO_2, H_2O, and H_2. The partial CO_2 pressure is around 20–25 bar and the temperature is around 573–623 K. To minimize the energy consumption, an ideal sorbent should work at these pressure and temperature ranges to separate CO_2 from H_2. We define a turnover temperature as the temperature above which the computed pressure of CO_2 exceeds that in the gas phase from which CO_2 is to be captured. For example, for a gas containing 20 bar pressure of CO_2 the turnover temperature would be the temperature at which the reactants and products are in equilibrium with a gas having a CO_2 partial pressure of 20 bar. We have estimated the turnover temperatures for pre-combustion conditions of these nine reactions from Figs. 2 to 4. These temperatures, denoted as T_1, are shown in Table 4. For post-combustion conditions, the gas stream mainly contains CO_2 and N_2, the partial pressure of CO_2 is around 0.1–0.2 bar, and the temperature range is quite bit lower (<473 K). From Figs. 2 to 4, we have also obtained the turnover temperatures for post-combustion capture and the corresponding values, denoted as T_2, are also shown in Table 4. Note that the partial pressure of H_2O in Fig. 4 is too high to be appropriate for post-combustion conditions. However, the effect of the partial pressure of water in going from 0.1 to 1 bar on the phase diagram is relatively small.

From Figs. 2 to 4 and Table 4, we see that all of the alkali oxides and hydroxides only can absorb CO_2 at very low CO_2 pressure and high temperature ranges which are far away from the pre- and post-combustion conditions. Therefore, none of these materials are good candidates for CO_2 sorbents. As one can see, the turnover temperature of the $Li_2CO_3/LiHCO_3$ system is lower than room temperature; therefore, it cannot be used in practical CO_2 capture technologies. However, the $Na_2CO_3/NaHCO_3$ and $K_2CO_3/KHCO_3$ reaction systems are very good candidates for CO_2 sorbents because these materials

Table 4
The highest temperatures for sorbents capturing CO_2 at pre-combustion (T_1) ($P_{H_2O}=20$ bar) and post-combustion (T_2) ($P_{CO_2}=0.1$ bar) conditions. For reactions involving H_2O, $P_{H_2O}=1$ bar.

Reactions	Pre-combustion **T_1 (K)**	Post-combustion **T_2 (K)**
$Li_2O+CO_2 \rightleftharpoons Li_2CO_3$	hT[a]	1290
$Na_2O+CO_2 \rightleftharpoons Na_2CO_3$	hT	hT
$K_2O+CO_2 \rightleftharpoons K_2CO_3$	hT	hT
$2LiOH+CO_2 \rightleftharpoons Li_2CO_3+H_2O(g)$	hT	hT
$2NaOH+CO_2 \rightleftharpoons Na_2CO_3+H_2O(g)$	hT	hT
$2KOH+CO_2 \rightleftharpoons K_2CO_3+H_2O(g)$	hT	hT
$Li_2CO_3+CO_2+H_2O(g) \rightleftharpoons 2LiHCO_3$	<300	<300
$Na_2CO_3+CO_2+H_2O(g) \rightleftharpoons 2NaHCO_3$	440	380
$K_2CO_3+CO_2+H_2O(g) \rightleftharpoons 2KHCO_3$	490	420

[a] hT means the maximum temperature exceeds our temperature range (1500 K).

have favorable turnover temperatures for both of pre- and post-combustion conditions. In fact, alkali carbonates are widely used for CO_2 capture either in aqueous or dry conditions [45,46]. The major advantage of carbonates/bicarbonates sorbents over amine-based sorbents is the significantly lower energy required for regeneration [17,47].

4. Conclusions

We have used first-principles density functional theory combined with phonon density of states calculations to obtain the phase diagrams of multi-component alkali metal M–C–O–H (M=Li, Na, K) systems. We have applied a linear program to compute the convex hull reactions for these systems and used the resulting data to estimate the thermodynamics of CO_2 capture reactions involving alkali metal oxides, hydroxides, and carbonates/bicarbonates. We have compared our calculations with pseudoexperimental data from both the HSC chemistry package and the JANAF tables. Our calculated data are seen to be in qualitative, and in some cases quantitative agreement with the HSC/JANAF data. Hence, in a purely predictive mode, DFT calculations may be used as a rough screening step to identify materials for CO_2 capture. The discrepancies between the DFT and pseudoexperimental data are likely due to four factors: (1) Errors in the calculated heats of formation of the compounds. (2) The assumption that the solids consist of perfect crystals throughout the temperature range. (3) The assumption that no solid–solid phase transitions take place for the pure solids (i.e. we use only one crystal structure for each of the distinct compounds). (4) The use of the harmonic approximation to compute the phonon dispersion relations for the crystals. Nevertheless, an important advantage of DFT methods is that it allows calculation of thermodynamic data for crystalline systems when they are not available from experimental measurements.

From the calculated phase diagrams of M–C–O–H (M=Li, Na, K) systems, we found that their oxides and hydroxides are not good candidates for CO_2 sorbents because the regenerating cycles only can occur at very low pressure or very high temperature. We predict that Na_2CO_3 and K_2CO_3 have turnover temperatures for CO_2 capture through bicarbonate formation that are suitable for operation under both pre- and post-combustion conditions.

Acknowledgment

This work was performed in support of the National Energy Technology Laboratory's Office of Research and Development under contract number DE-FE-0004000 with activity number 4000.2.660.241.001. One of us (YD) thanks Drs. S. Chen, Y. Soong, H. W. Pennline, and R. Siriwardane for fruitful discussions.

References

[1] D. Aaron, C. Tsouris, Sep. Sci. Technol. 40 (2005) 321–348.
[2] C.M. White, B.R. Strazisar, E.J. Granite, J.S. Hoffman, H.W. Pennline, J. Air Waste Manage. Assoc. 53 (2003) 645–715.
[3] M.R. Allen, D.J. Frame, C. Huntingford, C.D. Jones, J.A. Lowe, M. Meinshausen, N. Meinshausen, Nature 458 (2009) 1163–1166.
[4] H. Lund, B.V. Mathiesen, Energy 34 (2009) 524–531.
[5] E. Ochoa-Fernandez, H.K. Rusten, H.A. Jakobsen, M. Ronning, A. Holmen, D. Chen, Catal. Today 106 (2005) 41–46.
[6] H. Pfeiffer, P. Bosch, Chem. Mater. 17 (2005) 1704–1710.
[7] R.S. Haszeldine, Science 325 (2009) 1647–1652.
[8] J.C. Abanades, G. Grasa, M. Alonso, N. Rodriguez, E.J. Anthony, L.M. Romeo, Environ. Sci. Technol. 41 (2007) 5523–5527.
[9] S.C. Lee, H.J. Chae, S.J. Lee, B.Y. Choi, C.K. Yi, J.B. Lee, C.K. Ryu, J.C. Kim, Environ. Sci. Technol. 42 (2008) 2736–2741.
[10] S.C. Lee, B.Y. Choi, S.J. Lee, S.Y. Jung, C.K. Ryu, J.C. Kim, Stud. Surf. Sci. Catal. 153 (2004) 527–530.
[11] S.C. Lee, B.Y. Choi, T.J. Lee, C.K. Ryu, Y.S. Soo, J.C. Kim, Catal. Today 111 (2006) 385–390.
[12] V. Manovic, E.J. Anthony, Environ. Sci. Technol. 41 (2007) 1420–1425.
[13] M.M. Maroto-Valer, Z. Lu, Y. Zhang, Z. Tang, Waste Manage. 28 (2008) 2320–2328.
[14] R. Siriwardane, J. Poston, K. Chaudhari, A. Zinn, T. Simonyi, C. Robinson, Energy Fuels 21 (2007) 1582–1591.
[15] H.W. Pennline, D.R. Luebke, K.L. Jones, C.R. Myers, B.I. Morsi, Y.J. Heintz, J.B. Ilconich, Fuel Process. Technol. 89 (2008) 897–907.
[16] V. Nikulshina, N. Ayesa, M.E. Galvez, A. Steinfeld, Chem. Eng. J. 140 (2008) 62–70.
[17] S.C. Lee, J.C. Kim, Catal. Surv. Asia 11 (2007) 171–185.
[18] S.C. Lee, H.J. Chae, S.J. Lee, Y.H. Park, C.K. Ryu, C.K. Yi, J.C. Kim, J. Mol. Catal. B-Enzymatic 56 (2009) 179–184.
[19] Y. Duan, D.C. Sorescu, Phys. Rev. B 79 (2009) 014301.
[20] Y. Duan, D.C. Sorescu, J. Chem. Phys. 133 (2010) 074508.
[21] J.C. Abanades, E.J. Anthony, J. Wang, J.E. Oakey, Environ. Sci. Technol. 39 (2005) 2861–2866.
[22] G.X. Hu, H. Huang, Y.H. Li, Int. J. Hydrogen Energy 33 (2008) 5422–5429.
[23] B. Feng, H. An, E. Tan, Energy Fuels 21 (2007) 426–434.
[24] M.B. Jensen, L.G.M. Pettersson, O. Swang, U. Olsbye, J. Phys. Chem. B 109 (2005) 16774–16781.
[25] Y. Duan, A novel theoretical method to search good candidates of solid sorbents for CO_2 capture, in: Proceedings of the Seventh Annual Confererence on Carbon Capture and Sequestration, Pittsburgh, PA, May 5–8, 2008.
[26] H.A. Mosqueda, C. Vazquez, P. Bosch, H. Pfeiffer, Chem. Mater. 18 (2006) 2307–2310.
[27] A.R. Akbarzadeh, V. Ozolins, C. Wolverton, Adv. Mater. 19 (2007) 3233–3239.
[28] M.W.J. Chase, J. Phys. Chem. Ref. Data 9 (1998) 1–1951 Monograph.
[29] F. Gygi, G. Galli, Phys. Rev. B 52 (1995) R2229–R2232.
[30] M. Chaplin, Water Structure and Science, 2008. Available from: 〈http://www.lsbu.ac.uk/water〉.
[31] G. Kresse, J. Hafner, Phys. Rev. B 47 (1993) 558–561.
[32] G. Kresse, J. Furthmuller, Phys. Rev. B 54 (1996) 11169–11186.
[33] M.C. Payne, M.P. Teter, D.C. Allan, T.A. Arias, J.D. Joannopoulos, Rev. Mod. Phys. 64 (1992) 1045–1097.
[34] J.P. Perdew, Y. Wang, Phys. Rev. B 45 (1992) 13244–13249.
[35] H.J. Monkhorst, J.D. Pack, Phys. Rev. B 13 (1976) 5188–5192.
[36] M. Sternik, K. Parlinski, J. Chem. Phys. 122 (2005) 064707.
[37] K. Parlinski, Z.Q. Li, Y. Kawazoe, Phys. Rev. Lett. 78 (1997) 4063–4066.
[38] M. Sternik, K. Parlinski, J. Chem. Phys. 123 (2005) 204708.
[39] K. Parlinski, Software PHONON, 2006.
[40] C.J. Bradley, A.P. Cracknell, The Mathematical Theory of Symmetry in Solids, Clarendon Press, Oxford, 1972.
[41] J.C. Belmonte, J. Manzano, J. Arbiol, A. Cirera, J. Puigcorbe, A. Vila, N. Sabate, I. Gracia, C. Cane, J.R. Morante, Sensors Actuators B—Chem. 114 (2006) 881–892.
[42] A.D. Ryabtsev, L.T. Menzheres, A.A. Kurakov, E.P. Gushchina, Theor. Found. Chem. Eng. 40 (2006) 649–654.
[43] B. Baumeier, P. Kruger, J. Pollmann, Phys. Rev. B 76 (2007) 205404.
[44] H. Jacobs, J. Kockelkorn, T. Tacke, Z. Anorg. Allg. Chem. 531 (1985) 119–124.
[45] S.W. Park, D.H. Sung, B.S. Choi, J.W. Lee, H. Kumazawa, J. Ind. Eng. Chem. 12 (2006) 522–530.
[46] S.W. Park, D.H. Sung, B.S. Choi, K.J. Oh, K.H. Moon, Sep. Sci. Technol. 41 (2006) 2665–2684.
[47] J.D. Figueroa, T. Fout, S. Plasynski, H. Mcilvried, R.D. Srivastava, Int. J. Greenhouse Control 2 (2008) 9–20.
[48] T.W.D. Farley, W. Hayes, S. Hull, M.T. Hutchings, M. Vrtis, J. Phys.: Condens. Matter 3 (1991) 4761–4781.
[49] E. Zintl, A. Harder, B. Dauth, Z. Anorg. Allg. Chem. 198 (1931) 88–101.
[50] P. Touzain, F. Brisse, M. Caillet, Can. J. Chem. 48 (1970) 3358–3361.
[51] S.L. Mair, Acta Crystallogr. A 34 (1978) 542–547.
[52] Y. Idemoto, J.W. Richardson, N. Koura, S. Kohara, C.K. Loong, J. Phys. Chem. Solids 59 (1998) 363–376.
[53] I.P. Swaninson, M.T. Dove, M.J. Harris, J. Phys.: Condens. Matter 7 (1995) 4395–4417.
[54] B.D. Sharma, Acta Crystallogr. 18 (1965) 818–819.
[55] J.O. Thomas, R. Tellgren, I. Olovsson, Acta Crystallogr. B B30 (1974) 2540–2549.
[56] J.S. Hoffman, H.W. Pennline, Investigation of CO_2 capture using regenerable sorbents, in: Proceedings of the 17th Annual International Pittsburgh Coal Conference, Pittsburgh, September 11–15, 2000.
[57] R.D. Lide, CRC Handbook of Chemistry and Physics, 84th ed., CRC Press, 2003.